



Ge_{1-x}Sn_x Alloy Quantum Dots with Composition-Tunable Energy Gaps and Near-Infrared Photoluminescence

Journal:	<i>Nanoscale</i>
Manuscript ID	NR-ART-05-2018-004399.R1
Article Type:	Paper
Date Submitted by the Author:	22-Sep-2018
Complete List of Authors:	Tallapally, Venkatesham; Virginia Commonwealth University College of Humanities and Sciences, Department of Chemistry Nakagawara, Tanner ; Virginia Commonwealth University, Department of Electrical and Computer Engineering Demchenko, Denis ; Virginia Commonwealth University College of Humanities and Sciences, Department of Physics Ozgur, U.; Virginia Commonwealth University, Department of Electrical and Computer Engineering Arachchige, Indika; Viginia Commonwealth University, Chemistry



Ge_{1-x}Sn_x Alloy Quantum Dots with Composition-Tunable Energy Gaps and Near-Infrared Photoluminescence

Venkatesham Tallapally,¹ Tanner A. Nakagawara,² Denis O. Demchenko,³ Ümit Özgür,² and Indika U. Arachchige^{1}*

¹Department of Chemistry, Virginia Commonwealth University, Richmond, Virginia 23284, United States

²Department of Electrical and Computer Engineering, Virginia Commonwealth University, Richmond, Virginia 23284, United States

³Department of Physics, Virginia Commonwealth University, Richmond, Virginia 23284, United States

ABSTRACT

Low-cost, less-toxic, and abundantly-produced Ge_{1-x}Sn_x alloys are an interesting class of narrow energy-gap semiconductors that received noteworthy interest in optical technologies. Admixing of α -Sn into Ge results in an indirect-to-direct bandgap crossover significantly improving light absorption and emission relative to indirect-gap Ge. However, the narrow energy-gaps reported for bulk Ge_{1-x}Sn_x alloys have become a major impediment for their

widespread application in optoelectronics. Herein, we report the first colloidal synthesis of $\text{Ge}_{1-x}\text{Sn}_x$ alloy quantum dots (QDs) with narrow size dispersity (3.3 ± 0.5 – 5.9 ± 0.8 nm), wide range of Sn compositions (0–20.6%), and composition-tunable energy-gaps and near infrared (IR) photoluminescence (PL). The structural analysis of alloy QDs indicates linear expansion of cubic Ge lattice with increasing Sn, suggesting the formation of strain-free nanoalloys. The successful incorporation of α -Sn into crystalline Ge has been confirmed by electron microscopy, which suggests the homogeneous solid solution behavior of QDs. The quantum confinement effects have resulted in energy gaps that are significantly blue-shifted from bulk Ge for $\text{Ge}_{1-x}\text{Sn}_x$ alloy QDs with composition-tunable absorption onsets (1.72–0.84 eV for $x=1.5$ –20.6%) and PL peaks (1.62–1.31 eV for $x=1.5$ –5.6%). Time-resolved PL (TRPL) spectroscopy revealed microsecond and nanosecond timescale decays at 15 K and 295 K, respectively owing to radiative recombination of dark and bright excitons as well as the interplay of surface traps and core electronic states. Realization of low-to-non-toxic and silicon-compatible $\text{Ge}_{1-x}\text{Sn}_x$ QDs with composition-tunable near IR PL allows the unprecedented expansion of direct-gap Group IV semiconductors to a wide range of biomedical and advanced technological studies.

INTRODUCTION

Group-IV semiconductors show immense potential in a number of optical technologies including solar energy conversion, photo-detection, chemical sensing, and imaging.¹⁻⁴ However, indirect energy gaps of crystalline Si (1.1 eV) and Ge (0.67 eV) limit their widespread application in optical devices, significantly decreasing the absorption cross section and emission efficiency.^{2,3} Thus, a number of different methods, including application of mechanical stress,⁵ heteroepitaxial growth,⁶⁻⁸ and alloying with Sn,⁹⁻¹¹ have been investigated to produce direct

gap Group IV semiconductors with promising photophysical properties. Specifically, admixing of α -Sn into crystalline Si and Ge has been shown to decrease the energy of the Γ (direct) valley of conduction band relative to the L (indirect) valley producing direct bandgap $\text{Si}_{1-x}\text{Sn}_x$ or $\text{Ge}_{1-x}\text{Sn}_x$ alloys.⁸⁻¹² This transition stems from the expansion of cubic Si and Ge structure induced by α -Sn, the diamond-like structural equivalent to Si and Ge.¹² Theoretical and experimental reports suggest an indirect to direct-gap cross over in bulk $\text{Ge}_{1-x}\text{Sn}_x$ when Sn composition reaches 6.3–11%.¹⁰⁻¹⁵ In addition, incorporation of Sn enhances the electron and hole mobility, making direct-gap $\text{Ge}_{1-x}\text{Sn}_x$ alloys promising candidates for high speed optoelectronics.^{16,17} Unfortunately, the fabrication of homogeneous alloys has proven difficult, because of large discrepancies (~14-19%) in lattice constants and much higher cohesion energies of Si and Ge compared to that of α -Sn.¹⁸ Moreover, the admixture of α -Sn (bandgap (E_g) = 0.08 eV) significantly reduces the energy gaps (0.35–0.80 eV for $x = 15.0$ – 0.00 %)¹⁹ and promotes the metallic character of direct-gap $\text{Ge}_{1-x}\text{Sn}_x$ alloys, eliminating any potential application in visible to near IR optoelectronics.

To promote direct-gap behavior and expand the optical range, quantum confinement effects have been utilized to produce low-dimensional nanostructures of $\text{Ge}_{1-x}\text{Sn}_x$ alloys.²⁰⁻²⁴ Quantum dots (QDs) and nanowires (NWs) of $\text{Ge}_{1-x}\text{Sn}_x$ have been reported both at strongly-confined and weakly-confined size regimes that promote wider direct energy gaps from visible to near IR spectrum.^{17,20-27} Recently, our group reported the first colloidal synthesis of $\text{Ge}_{1-x}\text{Sn}_x$ alloy QDs with varying sizes (~2-23 nm) and Sn compositions ($x = 0$ –28%).²⁰ The larger $\text{Ge}_{1-x}\text{Sn}_x$ alloys (15–23 nm) exhibit minimum or no confinement effects and absorption energy gaps (0.2–0.4 eV) that are red-shifted from bulk Ge, similar to those reported for bulk $\text{Ge}_{1-x}\text{Sn}_x$ thin film alloys.

In contrast, smaller $\text{Ge}_{1-x}\text{Sn}_x$ alloy QDs ($\sim 2\text{--}5$ nm) show strong confinement effects with composition-tunable absorption onsets and visible PL, exclusively for ultra-small QDs (1.8–2.2 nm).^{20–23,28} A recent theoretical study suggests that admixture of $\alpha\text{-Sn}$ into Ge significantly increases the oscillator strengths, with the potential to produce brightly emissive QDs with high molar absorptivity and PL efficiency.²⁸ Nonetheless, size- and composition-dependent PL properties of near IR emitting $\text{Ge}_{1-x}\text{Sn}_x$ QDs have not been properly quantified to date, owing in part to high polydispersity of as-synthesized particles and significantly low PL quantum yields.²⁰ More recently, inorganic passivation of $\text{Ge}_{1-x}\text{Sn}_x$ QDs has been attempted to produce $\text{Ge}_{1-x}\text{Sn}_x/\text{CdS}$ core/shell QDs.²⁴ However, resultant alloys exhibit broad-band IR PL with no size (8–13 nm) or composition ($x = 5\text{--}25\%$) dependent tunability. As such, the synthesis of $\text{Ge}_{1-x}\text{Sn}_x$ alloys with enhanced near IR absorption and tunable near IR PL has proven a challenging task to further expand the optical window of direct-gap and silicon-compatible Group IV alloys.

Herein, we report the first colloidal synthesis of narrowly disperse ($3.3 \pm 0.5\text{--}5.9 \pm 0.8$ nm), near IR emitting (1.62–1.31 eV) $\text{Ge}_{1-x}\text{Sn}_x$ alloy QDs with wide range of Sn compositions ($x = 1.5\text{--}20.6\%$) via alkyllithium reduction of precursor halides (GeI_2 and SnCl_2). Control over QD diameter and composition was achieved by employing hexadecylamine (HDA) as the surfactant and changing the molar ratio of halides: reducing agent. The absorption energy gaps were tuned over a wide spectral region (1.72–0.84 eV) for narrowly disperse $\text{Ge}_{1-x}\text{Sn}_x$ QDs with $x = 1.5\text{--}9.1\%$. As-synthesized alloy QDs exhibit intense near IR emissions (1.62–1.31 eV for $x = 1.5\text{--}5.6\%$) and a clear red shift in PL energy with increasing Sn composition. It was found consistently that at room temperature (295 K) the PL decay of the alloy QDs was on the order of 10–20 ns, while it was ~ 3 orders of magnitude slower (1–10 μs) at low temperature (15 K). Such

temperature dependence of carrier dynamics suggests clearly distinguishable contributions from dark and bright excitons as well as the interplay between surface traps and core electronic states.

EXPERIMENTAL SECTION

Materials. Germanium diiodide (99.99+ %) and tin dichloride (99.9985 %) were purchased from Strem Chemicals and Alfa Aesar, respectively. n-butyllithium (BuLi, 1.6 M in hexane) was purchased from Sigma Aldrich. 1-octadecene (ODE, 90%) was purchased from Fisher Scientific. 1-Hexadecylamine (HDA), toluene, CCl₄, and methanol of ACS grade were purchased from Acros. ODE was dried at 120 °C under vacuum for 1 h. Methanol and toluene were dried over molecular sieves and Na, respectively and distilled under N₂ prior to use.

Synthesis of Ge_{1-x}Sn_x Alloy QDs. In a typical synthesis of 3–6 nm Ge_{1-x}Sn_x QDs, 3.00 g of HDA in a 50 mL three neck round bottom flask was fitted with a condenser and degassed under vacuum at 115 °C for 1 h. This set up was cooled to room temperature and transferred to a nitrogen glovebox. Then, appropriate amounts of GeI₂ and SnCl₂, 0.6 mmol of metal total, were combined with HDA and the sealed set up was connected to a Schlenk line. This mixture was degassed at 115 °C for 1 h to produce a homogeneous orange color solution. Then the reaction was flushed with nitrogen for 15 min and the temperature was raised to 230 °C, at which point 1.16–1.48 mmol (ESI, Table S1) of BuLi in 3.0 mL of ODE was swiftly injected. The injection caused a temperature drop to 209–213 °C and the mixture was reheated to 300 °C within 15 min to produce Ge_{1-x}Sn_x alloy QDs. The flask was then rapidly cooled with compressed air to ~100 °C and 10 mL of freshly distilled toluene was added. Then, 10 mL of freshly distilled methanol was added, followed by centrifugation at 4000g to precipitate the alloy QDs. The supernatant

was discarded and the QD precipitate was purified by dispersing in toluene and subsequent precipitation with methanol 2–3 times under ambient conditions.

Physical Characterization. The powder X-ray diffraction (PXRD) patterns were recorded using a PANanalytical X'pert PRO diffractometer calibrated with Si standard and equipped with Cu K α ($\lambda = 1.5418 \text{ \AA}$) radiation. Crystallite sizes were estimated by applying the Scherrer formula²⁹ to (111), (220), and (311) reflections of cubic Ge. Raman spectra were recorded on powder samples using a Horiba LABram HR Evolution Confocal Raman Spectrometer equipped with a 532 nm laser. The solid-state reflectance and solution-state absorption measurements were performed on a Cary 6000i UV-visible-near IR spectrophotometer (Agilent Technologies). Solid-state diffuse reflectance spectra were recorded by mixing QDs thoroughly with BaSO₄ powder and spreading them evenly on a BaSO₄ background holder. Kubelka-Munk remission function was employed to convert the measured reflectance to absorption.³⁰ The energy gaps were estimated from the intersection point of absorption onsets and the baseline of the absorption spectrum. A frequency doubled Ti: sapphire laser (385 nm wavelength, 150 fs pulse width, and 160 kHz to 80 MHz repetition rate) was utilized as the excitation source to record steady-state PL and TRPL spectra of QDs dispersed in CCl₄ as well as those drop-casted onto clean Si substrates. The elemental analysis was performed using a Hitachi FE-SEM Su-70 model scanning electron microscope (SEM) equipped with an energy dispersive spectroscopy (EDS) unit operating at 20 keV. Low resolution transmission electron microscopy (LRTEM) images were recorded on a JEOL JEM-1400 model microscope operating at 120 kV. High-resolution TEM (HRTEM) and Scanning TEM-energy dispersive spectroscopy (STEM-EDS) images were recorded on a FEI Titan 8300 microscope equipped with a Gatan 794 multiscan camera operating at 300 kV. Samples for TEM analysis were prepared by drop casting $\sim 5 \mu\text{L}$ of

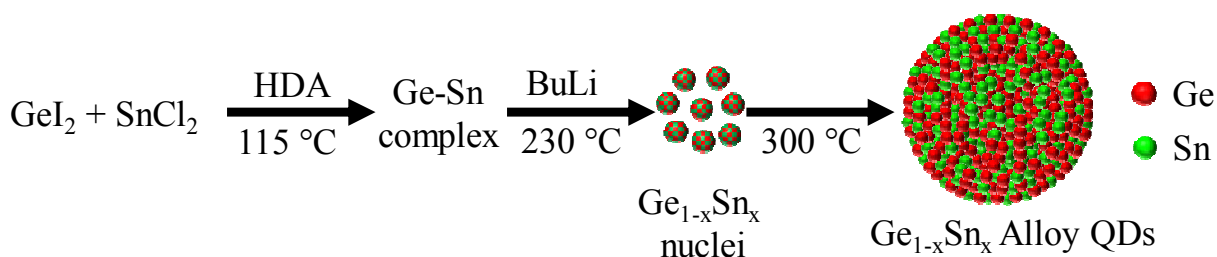
alloy QDs dispersed in hexane onto carbon-coated copper grids, followed by evaporation of the solvent. X-ray photoelectron (XPS) spectra were acquired on a ThermoFisher ESCALAB 250 instrument using Al K α radiation. XPS samples were prepared by pressing the powder samples onto indium foil (Sigma-Aldrich) prior to analysis. Sample surface charging was corrected to adventitious carbon and peak fits were performed with Thermo Advantage software. The infrared spectra of alloy QDs were recorded using a Nicolet 670 Fourier transform infrared (FT-IR) instrument equipped with a single reflection diamond ATR attachment.

RESULTS AND DISCUSSION

The lattice mismatch between Ge and Sn (~14%) causes a great challenge to produce homogeneous Ge_{1-x}Sn_x alloys.^{11,19} Because of its covalent bonding nature Ge requires high temperature (300-400 °C) to crystallize whereas Sn melts above 231 °C.³¹⁻³³ Hence these two elements are poorly miscible (~1% equilibrium solubility of Sn in bulk Ge) in the solid state. With consideration of aforementioned complications, we have developed a unique synthetic strategy to produce 3.3 ± 0.5 – 5.9 ± 0.8 nm Ge_{1-x}Sn_x alloy QDs with Sn content up to 20.6%. Colloidal synthesis provides a unique platform to incorporate significant Sn into Ge without altering its diamond cubic structure and simultaneously expanding the energy gaps owing to unique size confinement effects. Previous wet-chemical reports utilized oleylamine/octadecene as the surfactant/solvent and constant amount of reducing agent (n-butyllithium, BuLi) to produce 3.4–4.6 nm Ge_{1-x}Sn_x alloy QDs.²⁰ However, the fixed amount of n-BuLi resulted in minimum control over nanocrystal size (size dispersity = 15–25% for x = 0.0 – 11.0%) because Sn promotes the growth of larger polydisperse QDs.²⁰ Herein, by manipulating the nucleation and growth kinetics, a modified synthetic strategy has been developed to produce phase-pure Ge_{1-x}Sn_x alloy QDs with narrow size dispersity (11–15%) and nearly spherical morphology⁷

(Scheme 1). The size and composition of the alloy QDs were effectively controlled by varying the amount of n-BuLi across wide a range of Sn compositions (0.58–0.75 mmol of n-BuLi for $x = 20.6$ –1.5%) to equalize the growth effects of Sn.

Scheme 1. An Illustration of the Synthesis of Near Infrared Emitting $\text{Ge}_{1-x}\text{Sn}_x$ Alloy QDs.



Powder X-ray diffraction (PXRD) patterns of $\text{Ge}_{1-x}\text{Sn}_x$ alloy QDs indicate the phase purity of particles and Bragg reflections corresponding to diamond cubic Ge structure (Figure 1A). No diffraction peaks corresponding to GeO_2 , α -Sn, or β -Sn (tetragonal Sn) impurity phases were detected suggesting the production of homogeneous alloys. The major diffraction peaks were indexed to (111), (220), and (311) planes of diamond-cubic Ge (JCPDS # 01-089-5011). The peak broadening is quite significant as a result of Scherrer scattering, consistent with the synthesis of nanoalloys.²⁹ The crystallite sizes computed using Scherrer formula are in the range of 2.01 ± 0.2 – 3.82 ± 0.2 nm for $x = 1.5$ –20.6%. With increasing Sn, diffraction patterns shift to lower 2θ angles owing to expansion of cubic Ge structure by α -Sn. Unlike the bulk lattice constants, which show significant bowing, average lattice parameters calculated from diffraction patterns indicate near linear expansion of the cubic Ge structure with increasing Sn, consistent with the Vegard's rule (Figure 1B).³⁴ Lattice constants for cubic Ge and α -Sn are 5.66 and 6.49 Å, respectively. In contrast, as-synthesized alloy QDs exhibit intermediate lattice parameters of 5.64–5.85 Å, further supporting the synthesis of strain-free, homogeneous nanoalloys.

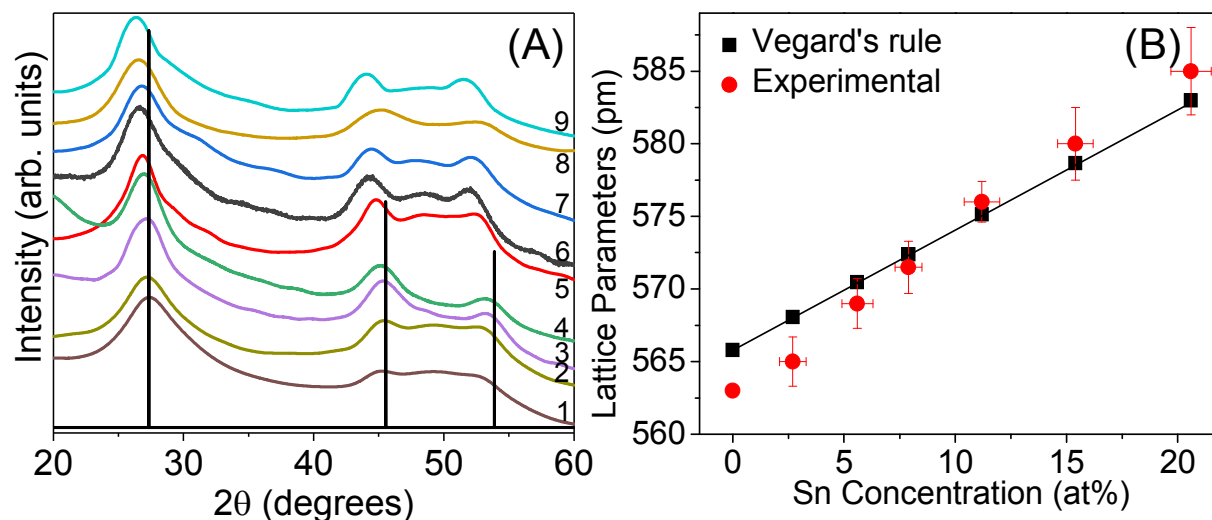


Figure 1. (A) PXR D patterns of $\text{Ge}_{1-x}\text{Sn}_x$ alloy QDs with varying Sn composition: (1) $x = 1.5\%$, (2) $x = 2.7\%$, (3) $x = 5.6\%$, (4) $x = 6.4\%$, (5) $x = 7.9\%$, (6) $x = 9.1\%$, (7) $x = 11.2\%$, (8) $x = 15.4\%$, and (9) $x = 20.6\%$. The ICDD-PDF overlay of diamond cubic Ge (JCPDS # 01-089-5011) is shown as vertical black lines. (B) A plot illustrating the variation of experimental (obtained from PXR D analysis) and theoretical (calculated using Vegard's rule) lattice parameters of selected QDs as a function of Sn composition. Experimental lattice parameters and Sn compositions were obtained from analysis of 3–5 individually prepared samples.

Raman spectroscopy was utilized to further study the alloying effects in $\text{Ge}_{1-x}\text{Sn}_x$ QDs. Crystalline Ge exhibits a Raman peak at 300 cm^{-1} that corresponds to the optical phonon mode of Ge–Ge bonds.³⁵ As heavier Sn atoms are incorporated into the Ge crystal, a systematic red shift of Ge–Ge phonon mode is expected.³⁵ Nonetheless, single element Ge QDs exhibit a broad, red shifted Ge–Ge peak at $297\text{--}300\text{ cm}^{-1}$ owing to phonon confinement effects.^{24,36} Therefore, the combined effects of phonon confinement and Sn induced shifting cannot be distinguished preventing quantification of Sn-induced expansion effects in the alloy. However, a systematic

red shift of the Ge–Ge phonon mode ($295\text{--}287\text{ cm}^{-1}$ for $x = 0.000\text{--}0.206$) with increasing heavier Sn atoms is observed for $3.3 \pm 0.5 - 5.9 \pm 0.8\text{ nm}$ alloy QDs, consistent with the weakening (or lengthening) of the Ge–Ge bond and lattice constants computed from Vegard's law (Figure 1B). The broadening of Ge–Ge peak is consistent with the increased alloy disorder and size confinement effects.^{21,37}

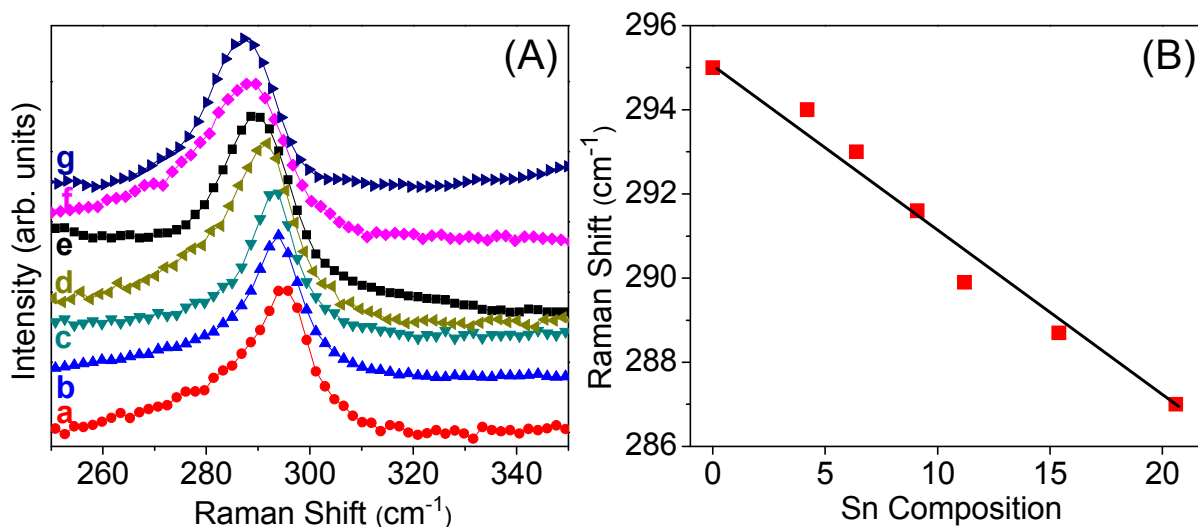


Figure 2. (A) Raman spectra of $\text{Ge}_{1-x}\text{Sn}_x$ alloy QDs with varying Sn compositions: (a) $x = 0.00\%$, (b) $x = 4.2\%$, (c) $x = 6.4\%$, (d) $x = 9.1\%$, (e) $x = 11.2\%$. (f) $x = 15.4\%$, and (g) $x = 20.6\%$. (B) A plot illustrating the systematic red-shifting of Ge–Ge optical phonon mode with increasing Sn composition.

TEM was used to investigate the morphology and size dispersity of alloy QDs. The LRTEM images of as-synthesized particles show narrow size dispersity ($3.3 \pm 0.5 - 5.9 \pm 0.8\text{ nm}$) and near spherical morphology across varying Sn compositions (Figure 3A–F). No size selective precipitation steps were employed during the isolation and purification of samples. A slight increase in particle size with increasing Sn composition was noted possibly due to Sn-induced growth of QDs.²⁰ The narrow size distribution of as-synthesized QDs was confirmed through

size analysis of 150–200 particles across multiple individually prepared samples, which yields dispersity of 11–15% (ESI, Figure S1-S3). In contrast, prior reports of $3.4 \pm 0.4 - 4.6 \pm 1.2$ nm $\text{Ge}_{1-x}\text{Sn}_x$ alloy QDs, produced in oleylamine, are reported to exhibit much higher size dispersity of 15–25%. The improved size and size dispersity control is attributed to strong interaction between $\text{Ge}_{1-x}\text{Sn}_x$ and HDA, which prevents the growth of larger polydisperse particles. In addition, HRTEM images of $\text{Ge}_{1-x}\text{Sn}_x$ alloy QDs indicate the single crystalline nature of particles with a lattice spacing of 3.32–3.41 Å for $x = 2.7\text{--}20.6\%$, consistent with an expanded (111) plane of cubic Ge (3.3 Å, ESI, Figure S4). The slight discrepancy in crystallite size estimated from PXRD and averaged particle size obtained from TEM analysis can be attributed to the presence of an amorphous $\text{Ge}_{1-x}\text{Sn}_x$ layer on the QD surface.

High-angle annular dark-field (HAADF) images and STEM-EDS elemental maps were utilized to probe the homogeneous solid solution behavior of $\text{Ge}_{1-x}\text{Sn}_x$ QDs. Elemental mapping of near IR emitting alloy QDs was difficult due to extremely small size ($3.3 \pm 0.5 - 5.9 \pm 0.8$ nm) and complete destruction of particles is often noted under the high energy beam. Therefore, a set of larger polydisperse (8-20 nm) alloy nanocrystals was produced, by extending the growth temperature (10 min.) at 300 °C, solely for STEM-EDS analysis. Elemental maps of 8–20 nm $\text{Ge}_{0.888}\text{Sn}_{0.112}$ alloy QDs indicate homogeneous distribution of Ge and Sn in the entire crystal, suggesting the solid solution behavior (Figure 4 and ESI, Figure S5). Therefore, the smaller near IR emitting alloy QDs, which act as seeds for the growth of larger polydisperse (8-20 nm) particles, should also be homogeneous, consistent with prior reports on colloiddally synthesized $\text{Ge}_{1-x}\text{Sn}_x$ nanoalloys.^{17,21,23,25,26} It should be noted while elemental maps were recorded from larger QDs that provide high counts from individual particles, the elemental composition of near

IR emitting alloy QDs were obtained from multiple individually prepared $3.3 \pm 0.5 - 5.9 \pm 0.8$ nm alloy particles and the average values are shown in Table 1.

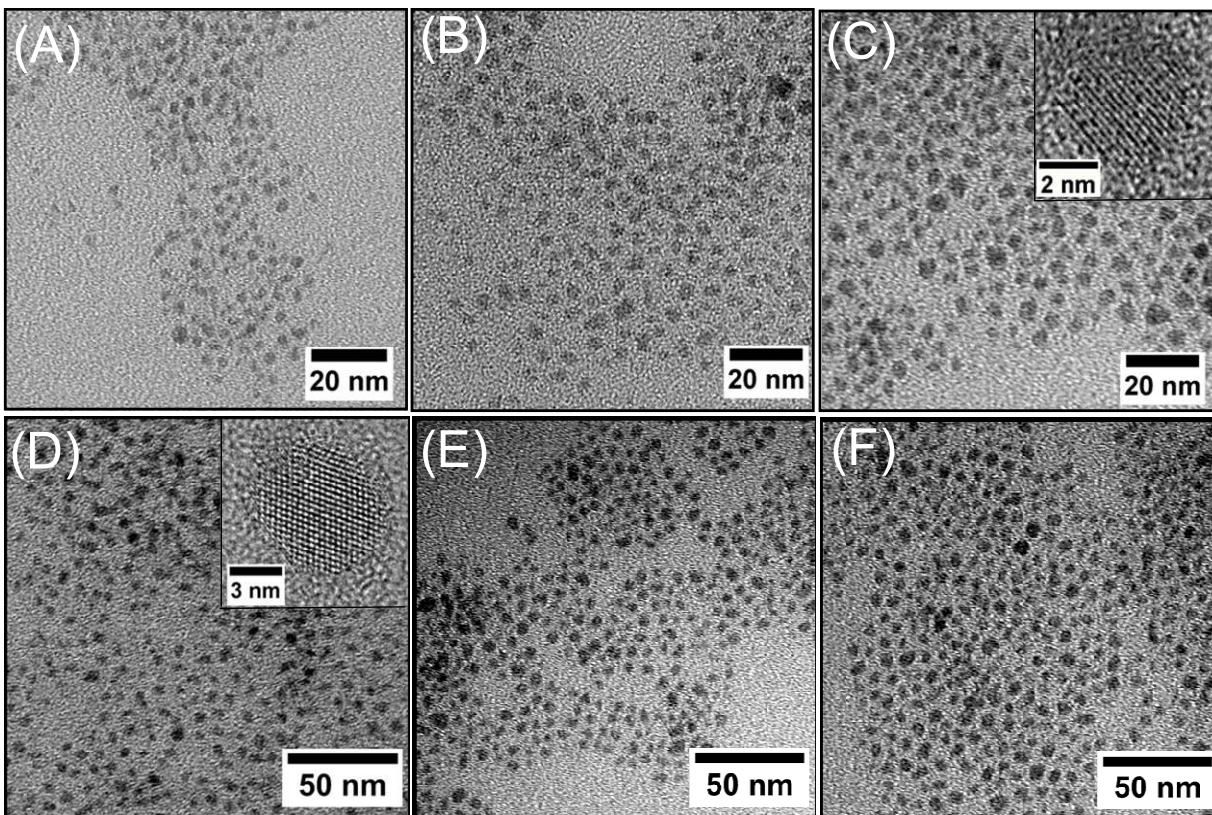


Figure 3. Representative low-resolution TEM images of $\text{Ge}_{1-x}\text{Sn}_x$ alloy QDs with varying Sn composition: (A) $x = 1.5\%$, (B) $x = 5.6\%$, (C) $x = 7.9\%$, (D) $x = 11.2\%$, (E) $x = 15.4\%$, and (F) $x = 20.6\%$. Insets in C and D show the high resolution TEM Images of selected QDs.

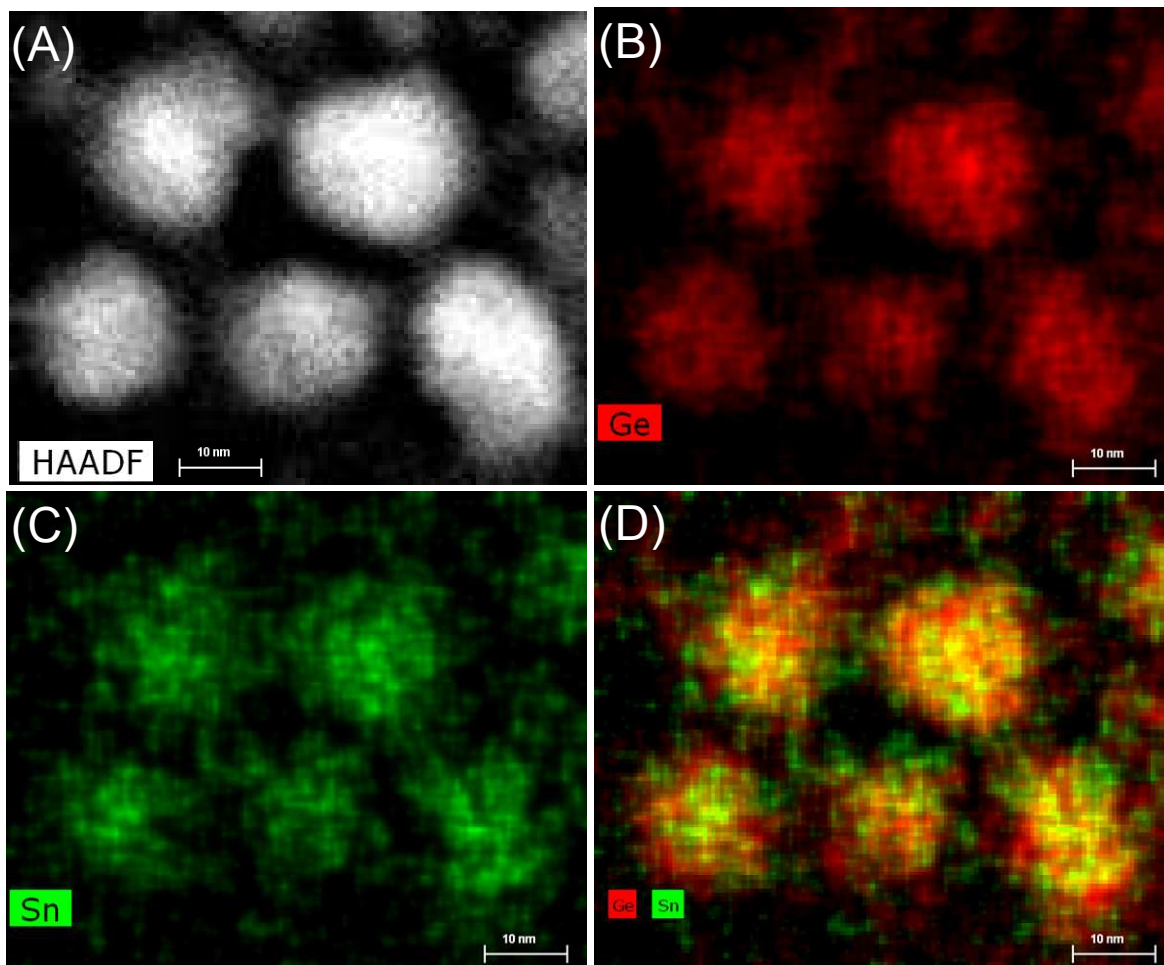


Figure 4. (A) Dark filed TEM image of 8–20 nm $\text{Ge}_{0.888}\text{Sn}_{0.112}$ alloy QDs along with STEM-EDS elemental maps of (B) Ge, (C) Sn, and (D) an overlay of Ge and Sn indicating the homogeneous distribution of elemental components throughout the alloy lattice.

The binding energies of Ge and Sn obtained from XPS spectra are consistent with prior reports of $\text{Ge}_{1-x}\text{Sn}_x$ nanoalloys (Figure 5).^{20,21} The survey XPS spectra exhibit peaks corresponding to Ge, Sn, C, and O with no other impurities, consistent with the EDS analysis (ESI, Figure S6 and S7). The peak at 28.4 eV in the Ge 3d_{5/2} spectra can be attributed to Ge(0), which has been shifted from the expected value of 29.4 eV, likely due to surface charging

effects.³⁸ The peak at 31.2 eV is likely arising from surface Ge^{2+} species coordinated to alkylamine and alkene passivating ligands.^{20,23} Consistent with XPS data, FTIR spectra of alloy QDs indicates the presence of HDA on QD surface (ESI, Figure S8). Occasionally, a minor peak at 34.0 eV is observed in Ge $3d_{5/2}$ spectra, which can be attributed to Ge^{4+} likely produced by surface oxidation (ESI, Figure S9). The examination of the Sn ($3d_{5/2}$) region indicates similar behavior with both core Sn^0 (483.9 eV) and surface $\text{Sn}^{2+/4+}$ (485.6 eV) species bound to stabilizing ligands.^{20,23,39,40} It is important to note that no GeO_x or SnO_x impurities were detected in PXRD and Raman spectra of QDs (Figure 1A and 2A). However, the presence of higher oxidation state peaks (*i.e.* Ge^{4+} and Sn^{4+} in particular) can also be attributed to minor oxide impurities produced via surface oxidation.^{20,21,23} Nonetheless, similar core and surface species were noted in Ge (3d and 2P) and Sn (3d) spectra of alloy QDs with varying Sn compositions, consistent with prior reports of $\text{Ge}_{1-x}\text{Sn}_x$ nanoalloys.^{20,21,23}

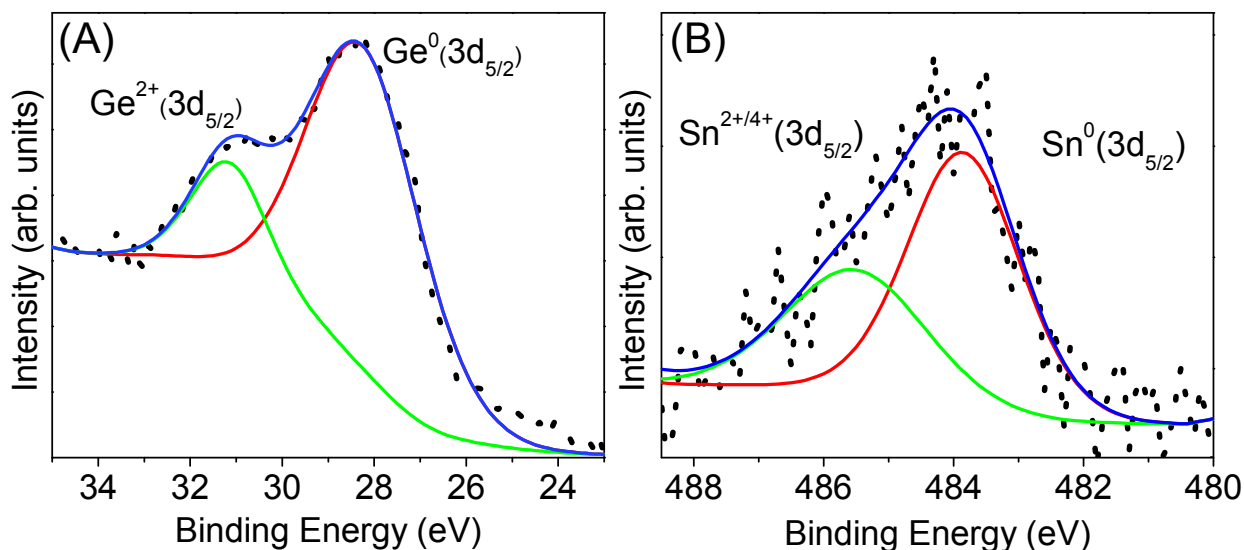


Figure 5. Representative (A) Ge ($3d_{5/2}$) and (B) Sn ($3d_{5/2}$) XPS spectra of $\text{Ge}_{0.888}\text{Sn}_{0.112}$ alloy QDs. Dotted lines represent the spectral data and the red and green lines are fitted deconvolutions of core Ge^0/Sn^0 and different oxidation states (Ge^{2+} , Sn^{2+} and Sn^{4+}) of surface species, respectively. Blue lines are spectral envelopes.

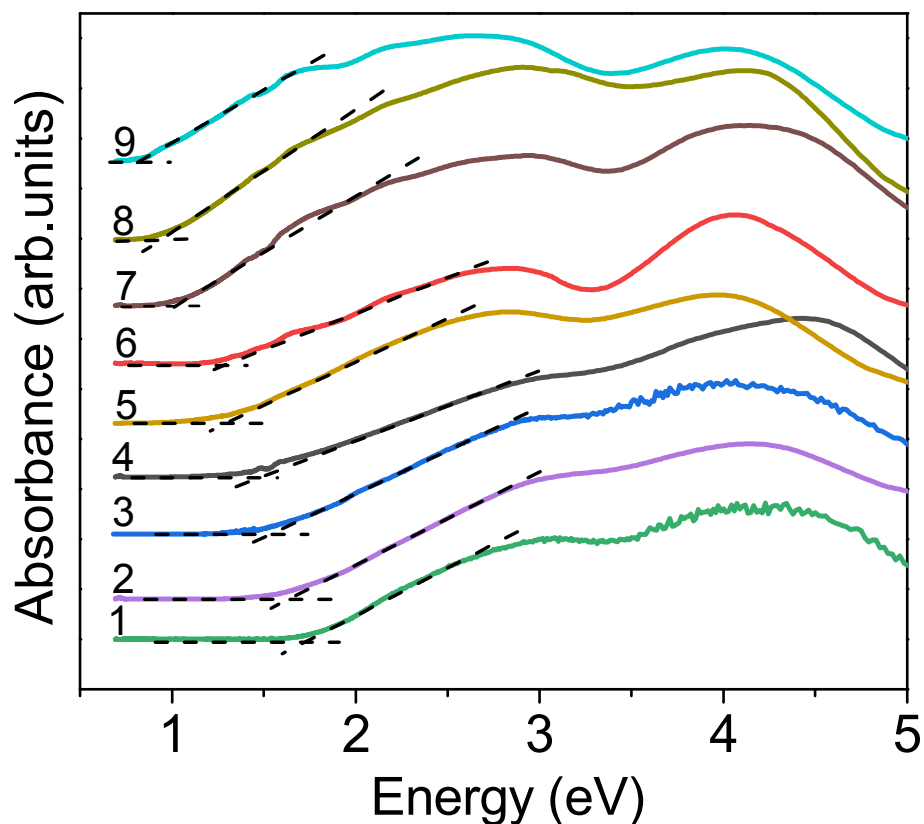


Figure 6. Solid state diffuse reflectance spectra (converted to absorption using Kubelka–Munk remission function) of $\text{Ge}_{1-x}\text{Sn}_x$ alloy QDs with varying Sn composition: (1) $x = 1.5\%$ (1.72 eV), (2) $x = 1.9\%$ (1.61 eV), (3) $x = 2.7\%$ (1.52 eV), (4) $x = 3.4\%$ (1.48 eV), (5) $x = 4.2\%$ (1.30 eV), (6) $x = 5.6\%$ (1.22 eV), (7) $x = 6.4\%$ (1.02 eV), (8) $x = 7.9\%$ (0.94 eV), and (9) $x = 9.1\%$ (0.84 eV). Corresponding absorption onset values are shown in parentheses.

Solid state diffuse reflectance (converted to absorption) spectroscopy was utilized to probe the absorption onsets of alloy QDs and effects of size confinement. The energy gaps obtained from Kubelka Munk³⁰ analysis indicate strong quantum confinement effects in $3.3 \pm 0.5 - 5.0 \pm 0.7$ nm $\text{Ge}_{1-x}\text{Sn}_x$ QDs with well-defined absorption onsets from 1.72–0.84 eV for $x = 1.5$ –9.1% compositions (Figure 6). A clear red-shift in absorption onset is noted with increasing Sn content for QDs with similar average size, consistent with Sn induced lowering of energy gaps. The

solid-state energy gaps of alloy QDs with higher Sn content ($x > 9.1\%$) could not be probed because of the instrumental limitations. Thus, solution absorption spectra were recorded to estimate the energy gaps over a wide range of Sn compositions (0–20.6%). Typical solution absorption spectra of $\text{Ge}_{1-x}\text{Sn}_x$ alloy QDs ($x = 1.5\text{--}20.6\%$, ESI, Figure S10) exhibit no excitonic peaks, consistent with prior reports on Ge and $\text{Ge}_{1-x}\text{Sn}_x$ QDs.^{20,23} However, the solution phase energy gaps estimated using Tauc function,^{1,23,30,41-43} yield values from 2.05–0.90 eV for $x = 1.5\text{--}20.6\%$ compositions (ESI, Figure S11). However, the energy gaps obtained from solid-state absorption spectra (Kubelka–Munk analysis) are in close agreement with the gap energies estimated from PL measurements (Figure 7 and Table 1). It should also be noted that both solid-state and solution-state energy gaps of $\text{Ge}_{1-x}\text{Sn}_x$ alloy QDs are significantly larger than those reported for bulk $\text{Ge}_{1-x}\text{Sn}_x$ thin film alloys (0.35–0.80 eV for $x = 15.0\text{--}0.00\%$),¹⁹ consistent with the expected quantum confinement effects.

Table 1. Comparison of the Elemental Composition, Crystallite and Primary Particle Size, and Room Temperature Solid-State Absorption Onsets and Photoluminescence Peak maxima for $3.3 \pm 0.5 - 5.9 \pm 0.8$ nm $\text{Ge}_{1-x}\text{Sn}_x$ Alloy QDs.

Sample	Sn Composition (x) ^a	Particle Size (nm) ^b	Crystallite Size ^c (nm)	Energy gap (eV) ^d	PL Peak Position (eV)
1	0.015	3.3 ± 0.5 nm	1.9 ± 0.2	1.72	1.62
2	0.019	3.4 ± 0.5 nm	2.1 ± 0.2	1.61	1.52
3	0.027	3.5 ± 0.6 nm	2.2 ± 0.2	1.52	1.43
4	0.034	3.7 ± 0.5 nm	2.4 ± 0.2	1.48	1.38
5	0.042	3.9 ± 0.6 nm	2.8 ± 0.2	1.30	1.34
6	0.056	4.4 ± 0.7 nm	2.8 ± 0.2	1.22	1.31
7	0.064	4.5 ± 0.6 nm	2.9 ± 0.2	1.02	n/a ^f
8	0.079	4.6 ± 0.8 nm	3.0 ± 0.3	0.94	n/a ^f
9	0.091	5.0 ± 0.7 nm	3.3 ± 0.2	0.84	n/a ^f
10	0.112	5.2 ± 0.6 nm	3.5 ± 0.3	n/a ^e	n/a ^f
11	0.154	5.5 ± 0.8 nm	3.6 ± 0.3	n/a ^e	n/a ^f
12	0.206	5.9 ± 0.8 nm	3.8 ± 0.2	n/a ^e	n/a ^f

^aElemental compositions of Ge and Sn were obtained from SEM/EDS analysis of multiple individually prepared samples and the averaged values obtained from 5 individual measurements for each sample are presented. ^bAverage particle sizes were calculated from 150–200 individual QDs from TEM images of multiple individually prepared samples. ^cCrystallite sizes were calculated by applying the Scherrer formula to (111), (220), and (311) reflections of PXRD patterns and average values are presented. ^dEnergy gaps were estimated from extrapolating the first major absorption onset to the intersection point of the baseline using linear fits. ^eOnset cut off due to detector limitation. ^fNo detectable PL was noted.

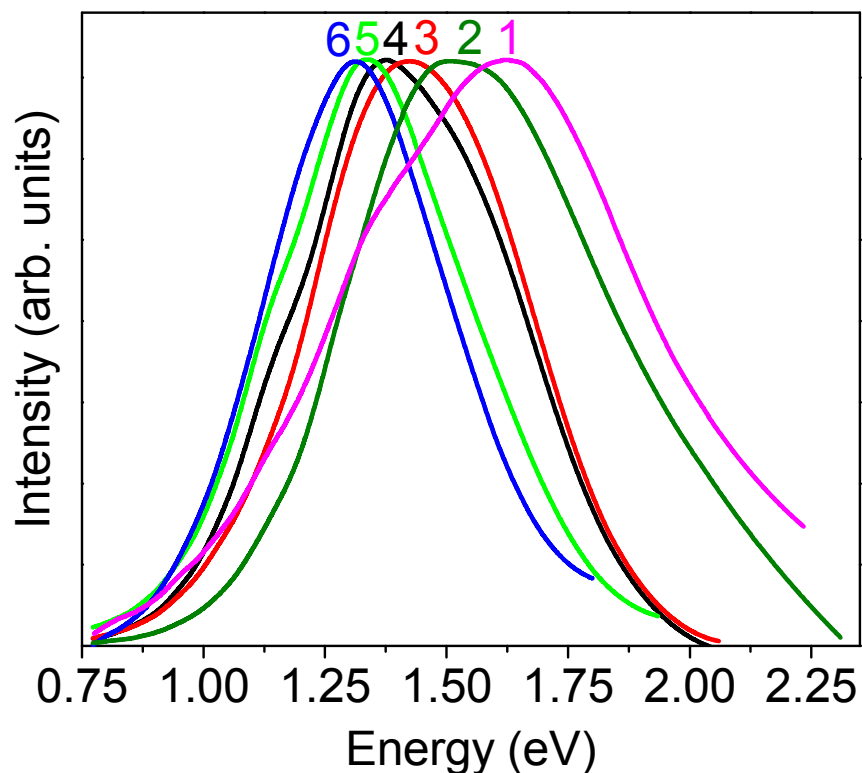


Figure 7. Room-temperature solid-state photoluminescence spectra of $\text{Ge}_{1-x}\text{Sn}_x$ alloy QDs with varying Sn compositions: (1) $x = 1.5\%$ (1.62 eV), (2) $x = 1.9\%$ (1.52 eV), (3) $x = 2.7\%$ (1.43 eV), (4) $x = 3.4\%$ (1.38 eV), (5) $x = 4.2\%$ (1.34 eV), and (6) $x = 5.6\%$ (1.31 eV). Corresponding PL peak maxima are shown in parentheses.

Solid-state emission spectra of $\text{Ge}_{1-x}\text{Sn}_x$ alloy QDs exhibit composition tunable PL peak energies in the near IR spectrum (1.62–1.31 eV for $x = 0.015$ – 0.056 , Figure 7). Consistent with absorption studies, a clear red shift in PL maxima was noted with increasing Sn composition. The PL peak energies are red shifted from those reported for ultra-small (1.8–2.2 nm) $\text{Ge}_{1-x}\text{Sn}_x$ alloy QDs (2.0–1.72 eV for $x = 1.8$ – 23.6%), owing to larger particles produced in the current study.^{21, 22} It is important to note that this is the first report on tunable near IR emitting $\text{Ge}_{1-x}\text{Sn}_x$ alloy QDs with wide range of Sn compositions. Previous studies on 6–11 nm $\text{Ge}_{1-x}\text{Sn}_x/\text{CdS}$

core/shell QDs with 5 and 25% Sn compositions showed broad-band PL (800–1200 nm) with no tunability as a function of size or composition.²⁴ Likewise, larger (9–10 nm) $\text{Ge}_{1-x}\text{Sn}_x$ alloy QDs with high Sn content ($x = 36\text{--}39\%$) are reported to exhibit broad and weak PL in the deep IR region ($\sim 0.45\text{--}0.55$ eV).²³ In contrast, alloy QDs reported in this study exhibit wide tunability of near IR PL across different Sn compositions. Moreover, the solid-state absorption onsets are in close agreement with the PL peak maxima, suggesting that the PL results from fundamental energy gap transitions (ESI, Figure S12). The solution-state PL spectra are slightly weaker than those reordered from solid-state samples because of the lower excitation powder used in solution-state analysis. However, both solution-state and solid-state PL spectra show consistent PL peak maxima with varying excitation energy, suggesting that emission results from inter-band electronic transitions of alloy QDs (ESI, Figure S13 and S14).^{44,45} However, PL from QDs with Sn content higher than 5.6% could not be probed possibly due to poor surface passivation and/or weaker confinement effects, resulting in higher degree of non-radiative recombination. As such, efforts are currently underway to utilize different surface passivation strategies to eliminate surface defects, enhanced the PL efficiency, and improve the chemical and optical stability of QDs with higher Sn compositions.

To investigate carrier relaxation pathways and further understand the origin of near IR PL, temperature dependent time-resolved PL experiments were performed. Figure 8 shows the PL transients measured for $\text{Ge}_{1-x}\text{Sn}_x$ alloy QDs with $x = 1.9\%$, 4.2% , and 5.6% at 295 K and 15 K. All transients are well described by biexponential decay fits, providing fast decay constants of $\tau_{\text{fast}} = 8\text{--}11.7$ ns and slow decay constants of $\tau_{\text{slow}} = 80\text{--}119$ ns at room temperature (295 K, Table 2). In contrast, the PL decays are much slower at 15 K: $\tau_{\text{fast}} = 1\text{--}1.6$ μs , $\tau_{\text{slow}} = 7.8\text{--}10.8$

μs . This drastic difference can be explained by a combined effect of surface trap states and dark-bright exciton splitting in QDs.^{21,22} The spin-forbidden dark exciton recombination is slow at 15 K, and increased thermal energy at room temperature makes bright excitonic states accessible, improving the recombination rates. Moreover, slow recombination at 15 K may also be partially due to charge trapping at the surface states, which can lead to long carrier times owing to separation of photoexcited carriers. Nearly an order of magnitude reduction in PL intensities at 295K compared to those at 15 K suggests a dominant role of nonradiative recombination at increased temperatures. While it is outside the scope of this report, further studies are currently underway to differentiate the individual contributions from different carrier relaxation pathways to better understand the origin of near IR PL.

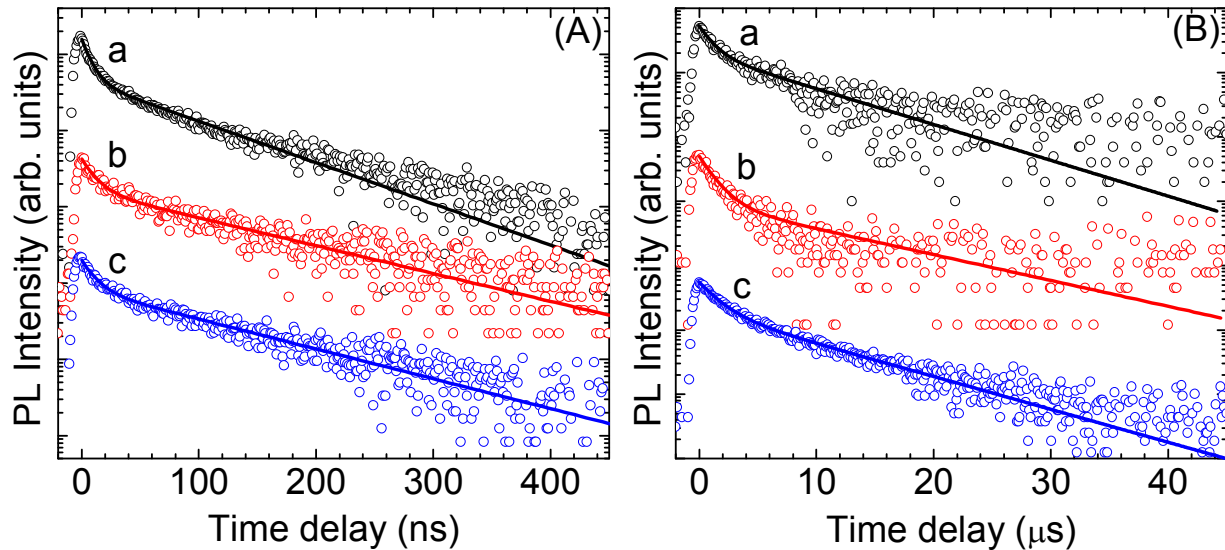


Figure 8. PL transients at (A) 295 K and (B) 15 K for $\text{Ge}_{1-x}\text{Sn}_x$ alloy QDs with varying Sn compositions: (a) $x = 1.9\%$, (b) $x = 4.2\%$, and (c) $x = 5.6\%$. The solid lines are biexponential fits.

Table 2. Time Constants Extracted from Biexponential Decay Fits ($A_{fast} e^{-t/\tau_{fast}} + A_{slow} e^{-t/\tau_{slow}}$) to PL Transients of Near IR Emitting $Ge_{1-x}Sn_x$ Alloy QDs.

@295 K	τ_{fast} (ns)	τ_{slow} (ns)	A_{fast}/A_{slow}
x = 0.019	8.0 ± 0.2	80.2 ± 1.3	2.44
x = 0.042	11.7 ± 0.8	119.1 ± 4.2	1.54
x = 0.056	11.5 ± 0.6	111.1 ± 2.7	1.41
@15 K	τ_{fast} (μ s)	τ_{slow} (μ s)	A_{fast}/A_{slow}
x = 0.019	1.1 ± 0.1	7.8 ± 0.4	1.64
x = 0.042	1.3 ± 0.1	10.8 ± 1.1	4.27
x = 0.056	1.6 ± 0.1	8.5 ± 0.2	1.78

CONCLUSIONS

In conclusion, for the first time we have successfully produced narrowly disperse $Ge_{1-x}Sn_x$ alloy QDs with wide tunability of Sn compositions (0–20.6%) and composition-tunable near IR absorption and intense PL. The diameter of alloy QDs was tuned by varying the molar ratio of precursor halides: n-BuLi minimizing the size dispersity to ~11-15%, across varying Sn compositions. The lattice parameters computed from PXRD analysis indicate near linear expansion of diamond cubic Ge structure with increasing Sn content, suggesting the formation of strain-free nanoalloys. The successful incorporation of α -Sn into cubic Ge has been further confirmed by PXRD patterns, STEM-EDS elemental maps, and Raman spectroscopy studies. The quantum confinement effects have resulted in energy gaps that are significantly blue-shifted from bulk $Ge_{1-x}Sn_x$ thin film counterparts for alloy QDs with composition-tunable absorption

onsets (1.72–0.84 eV for $x = 1.5$ –20.6%) and PL maxima (1.62–1.31 eV for $x = 1.5$ –5.6%) primarily in the near IR spectrum. The temperature dependent TRPL spectroscopy suggests microsecond and nanosecond PL decays at 15 K and 295 K, respectively owing to radiative recombination of dark and bright excitons and carriers trapped at surface states. The colloidal synthesis reported here has expanded the optical window of direct-gap $\text{Ge}_{1-x}\text{Sn}_x$ alloy QDs into near IR spectrum allowing less-toxic, earth abundant, and silicon-compatible Group IV elements for application in a broad range of electronic and photonic technologies.

ASSOCIATED CONTENT

The Electronic Supplementary Information (ESI) is available: Molar ratios of GeI_2 : SnCl_2 : n -BuLi used in the synthesis of $\text{Ge}_{1-x}\text{Sn}_x$ alloy QDs, Size histograms of $3.3 \pm 0.5 - 5.9 \pm 0.8$ nm $\text{Ge}_{1-x}\text{Sn}_x$ alloy QDs, LRTEM and HRTEM images of $\text{Ge}_{1-x}\text{Sn}_x$ alloy QDs ($x = 1.5$ –20.6%), STEM/EDS elemental maps of $\text{Ge}_{0.919}\text{Sn}_{0.091}$ alloy QDs, EDS spectrum of $\text{Ge}_{0.909}\text{Sn}_{0.091}$ alloy QDs, XPS of $\text{Ge}_{0.888}\text{Sn}_{0.112}$ (survey scan) and $\text{Ge}_{0.909}\text{Sn}_{0.091}$ alloy QDs, FT-IR and solution-state absorption spectra (Tauc analysis) of $\text{Ge}_{1-x}\text{Sn}_x$ alloy QDs, and solid state absorption onset and PL peak maxima of $\text{Ge}_{1-x}\text{Sn}_x$ alloy QDs with Sn varying composition ($x = 1.5$ –5.6%).

AUTHOR INFORMATION

Corresponding Author

*Indika U. Arachchige; E-mail: iuarachchige@vcu.edu

Author Contributions

The manuscript was written through contributions of all authors. All authors have given approval to the final version of the manuscript.

Conflicts of Interest

The authors declare no conflict of interests.

ACKNOWLEDGMENTS

Authors acknowledge Dr. Liu for the assistance of STEM at North Carolina State University, which is supported by the State of North Carolina and the National Science Foundation. Authors gratefully acknowledge the U.S. National Science Foundation (DMR-1506595) for financial support.

REFERENCES

1. D. A. Ruddy, J. C. Johnson, E. R. Smith and N. R. Neale, *ACS Nano*, 2010, **4**, 7459–7466.
2. A. P. Alivisatos, *Science*, 1996, **271**, 933–937.
3. M. C. Beard, K. P. Knutsen, P. Yu, J. M. Luther, Q. Song, W. K. Metzger, R. J. Ellingson and A. J. Nozik, *Nano Lett.*, 2007, **7**, 2506–2512.
4. D. D. Vaughn, II. and R. E. Schaak, *Chem. Soc. Rev.*, 2013, **42**, 2861–2879.
5. C. Boztug, J. R. Sanchez-Perez, F. Cavallo, M. G. Lagally and R. Paiella, *ACS Nano*, 2014, **8**, 3136–3151.
6. D. Nam, D. S. Sukhdeo, S. Gupta, J.-H. Kang, M. L. Brongersma and K. C. Saraswat, *IEEE J. Sel. Topics Quantum Electron.*, 2014, **20**, 1500107/1–1500107/7.
7. M. J. Suess, R. Geiger, R. A. Minamisawa, G. Schiefler, J. Frigerio, D. Chrastina, G. Isella, R. Spolenak, J. Faist and H. Sigg, *Nat. Photonics*, 2013, **7**, 466–472.
8. J. Tolle, A. V. G. Chizmeshya, Y.-Y. Fang, J. Kouvetakisa, V. R. D’Costa, C.-W. Hu, J. Menéndez and I. S. T. Tsong, *Appl. Phys. Lett.*, 2006, **89**, 231924/1–231924/3.

9. N. Bhargava, M. Coppinger, J. P. Gupta, L. Wielunski and J. Kolodzey, *Appl. Phys. Lett.*, 2013, **103**, 041908/1–041908/4.
10. S. Gupta, R. Chen, Y.-C. Huang, Y. Kim, E. Sanchez, J. S. Harris and K. C. Saraswat, *Nano Lett.*, 2013, **13**, 3783–3790.
11. S. Gupta, B. Magyari-Koepe, Y. Nishi and K. C. Saraswat, *J. Appl. Phys.*, 2013, **113**, 073707/1–073707/7.
12. B. Wang, G. Ouyang, Y. H. Yang and G. W. Yang, *Appl. Phys. Lett.*, 2007, **90**, 121905/1–121905/3.
13. R. Chen, H. Lin, Y. Huo, C. Hitzman, T. I. Kamins and J. S. Harris, *Appl. Phys. Lett.*, 2011, **99**, 181125/1–181125/3.
14. M.-H. Lee, P.-L. Liu, Y.-A. Hong, Y.-T. Chou, J.-Y. Hong and Y.-J. Siao, *J. Appl. Phys.*, 2013, **113**, 063517/1–063517/5.
15. N. Yahyaoui, N. Sfina, J.-L. Lazzari, A. Bournel and M. Said, *J. Appl. Phys.*, 2014, **115**, 033109/1–033109/9.
16. L. Liu, R. Liang, J. Wang and J. Xu, *Appl. Phys. Express*, 2015, **8**, 031301/1–031301/4.
17. M. S. Seifner, S. Hernandez, J. Bernardi, A. Romano-R and S. Sven Barth, *Chem. Mater.*, 2017, **29**, 9802–9813.
18. C. Kittel, *Wiley: Hoboken, NJ*, 2005, P50.
19. R. Ragan, K. S. Min and H. A. Atwater, *Mater. Sci. Eng.*, 2001, **79**, 1937–1940.
20. R. J. A. Esteves, M. Q. Ho and I. U. Arachchige, *Chem. Mater.*, 2015, **27**, 1559–1568.
21. R. J. A. Esteves, S. Hafiz, D. O. Demchenko, U. Ozgur and I. U. Arachchige, *Chem. Commun.*, 2016, **52**, 11665–11668.

22. S. A. Hafiz, R. J. A. Esteves, D. O. Demchenko, I. U. Arachchige and Ü. Özgür, *J. Phys. Chem. Lett.*, 2016, **7**, 3295–3301.
23. K. Ramasamy, P. G. Kotula, A. F. Fidler, M. T. Brumbach, J. M. Pietryga and S. A. Ivanov, *Chem. Mater.*, 2015, **27**, 4640–4649.
24. B. W. Boote, L. Men, H. P. Andaraarachchi, U. Bhattacharjee, J. W. Petrich, J. Vela and E. A. Smith, *Chem. Mater.*, 2017, **29**, 6012–6021.
25. M. S. Seifner, F. Biegger, A. Lugstein, J. Bernardi and S. Barth, *Chem. Mater.*, 2015, **27**, 6125–6130.
26. S. Barth, M. S. Seifner and J. Bernardi, *Chem. Commun.*, 2015, **51**, 12282–12285.
27. S. Biswas, J. Doherty, D. Saladukha, Q. Ramasse, D. Majumdar, M. Upmanyu, A. Singha, T. Ochalski, M. A. Morris and J. D. Holmes, *Nat. Commun.*, 2016, **7**, 11405/1–11405/5.
28. D. O. Demchenko, V. Tallapally, R. J. A. Esteves, S. Hafiz, T. A. Nakagawara, I. U. Arachchige and Ü. Özgür, *J. Phys. Chem. C*, 2017, **121**, 18299–18306.
29. H. Borchert, E. V. Shevehenko, A. Robert, I. Mekis, A. Kornowski, G. Grubel and H. Weller, *Langmuir*, 2005, **21**, 1931–1936.
30. M. Nowak, B. Kauch and P. Szperlich, *Rev. Sci. Instrum.*, 2009, **80**, 046107/1–046107/3.
31. K. Tabatabaei, H. Lu, B. M. Nolan, X. Cen, C. E. McCold, X. Zhang, R. L. Brutchey, K. V. Benthem, J. Hihath and S. M. Kauzlarich, *Chem. Mater.*, 2017, **29**, 7353–7363.
32. S. R. Herd, P. Chaudhari and M. H. Brodsky, *J. Non-Cryst. Solids*, 1972, **7**, 309–327.
33. D. D. Vaughn II, J. F. Bondi and R. E. Schaak, *Chem. Mater.*, 2010, **22**, 6103–6108.
34. A. V. G. Chizmeshya, M. R. Bauer and J. Kouvetakis, *Chem. Mater.*, 2003, **15**, 2511–2519.

35. V. A. Volodin, D. V. Marin, V. A. Sachkov, E. B. Gorokhov, H. Rinnert and M. Vergnat, *J. Exp. Theor. Phys.*, 2014, **118**, 65–71.
36. K. S. Oh, K.-W. Yang, H. T. Kim, H. Lee, J. C. Lee and Y.-S. Sohn, *J. Nanoelectron. Optoelectron.*, 2013, **8**, 571–574.
37. A. Tsuge, Y. Uwamino, T. Ishizuka and K. Suzuki, *Appl. Spectrosc.*, 1991, **45**, 1377–1380.
38. K. K. Kalebaila, D. G. Georgiev and S. L. Brock, *J. Non-Cryst. Solids*, 2006, **352**, 232–240.
39. D. Devaiah, T. Tsuzuki, T. Boningari, P. G. Smirniotisc and B. M. Reddy, *RSC Adv.*, 2015, **5**, 30275–30285
40. V. Tallapally, R. J. A. Esteves, L. Nahar and I. U. Arachchige, *Chem. Mater.*, 2016, **28**, 5406–5414.
41. J. Tauc, R. Grigorovici and A. Vancu, *Phys. Status Solidi*, 1966, **15**, 627–637.
42. A. J. Biacchi, D. D. Vaughn and R. E. Schaak, *J. Am. Chem. Soc.*, 2013, **135**, 11634–11644.
43. S. Ganguly, N. Kazem, C. Danielle and S. M. Kauzlarich, *J. Am. Chem. Soc.*, 2014, **136**, 1296–1299.
44. J. Hoy, P. J. Morrison, L. K. Steinberg, W. E. Buhro, R. A. Loomis, *J. Phys. Chem. Lett.*, 2013, **4**, 2053–2060.
45. P. Xiao, J. Lou, H. Zhang, W. Song, X.-L. Wu, H. Lin, J. Chen, S. Liuc, X. Wang, *Catal. Sci. Technol.*, 2018, **8**, 201–209.

Table of Contents

Colloidal synthesis and photophysical characterization of silicon-compatible $\text{Ge}_{1-x}\text{Sn}_x$ alloy quantum dots with composition-tunable near infrared absorption and photoluminescence is reported.

